small structures
www.small-structures.com

Highly Porous NiFe Nanofoams Synthesized by Dynamic Hydrogen Bubble Template for Hydrogen Evolution in Alkaline Media

Gabriel Garcia Carvalho, Ricardo Espingardas do Nascimento, Maria Teresa Silva, and Maria de Fátima Montemor*

When coupled with renewable energy sources, alkaline electrolysis (AEL) is a clean technology to produce hydrogen. The conventional electrodes that have been established as the commercial standard for AEL are perforated nickel plates, which have low surface area and high mass loads of active material. The use of Ni has been associated with the adsorption of protons and their recombination into H_2 molecules, assisting and enabling the hydrogen evolution reactions. Due to the rising Ni price, there is a demand for less expensive electrode materials with identical, or better, performance. Thus, this work explores new alternative electrode materials and combines Ni with a cheaper and also electroactive metal, iron. For this purpose, highly porous bimetallic nanofoams are produced through the dynamic hydrogen bubble template. NiFe electrodes of different compositions are characterized by scanning electron microscopy, energy-dispersive spectroscopy, linear sweep voltammetry, and chronopotentiometry analysis. The results allow obtaining key parameters that are essential for the optimization of the electrode's response considering overpotentials, Tafel slopes, and other electrochemically relevant parameters.

1. Introduction

In the scope of the energy transition, hydrogen becomes an important player due to the attractive promise of clean synthesis and clean combustion, being strategically placed within the key pillars set for 2050 decarbonization goals. Globally, 83% of hydrogen production is from processes dependent on fossil fuels (i.e., natural gas, coal) through steam reforming of methane and hydrocarbon pyrolysis, while 16% is produced as an industrial by-product, and only about 0.7% is produced using low-emission routes.[1–3] These figures evidence how important the decarbonization of the hydrogen industry is. Considering renewable energy sources and their potential surplus, electricity can be used in the water electrolysis to split water molecules into hydrogen and oxygen via reduction and oxidation reactions, respectively. If the energy source is renewable and of carbon-zero nature, then the rest of the electrolysis process is also guaranteed to be sustainable and carbon-free.

Alkaline electrolysis (AEL) remains the most commercially available and mature electrolysis technology in the world due to its simplicity and robustness. Several optimization strategies, such as the use of bipolar cell stacks, zero gap designs (in which the distance between the separation membrane and the electrodes is eliminated), and other advances, have been focused on the minimization of the ohmic resistances of the electrolysis process.[4,5] However, in addition to these, the development of novel and efficient electrodes heavily impacts the overall performance of the electrolyzer by defining and optimizing the kinetics and mechanisms of hydrogen production.

Among the best-performing materials for hydrogen evolution, Pt excels as electrode catalyst. The excellent electrocatalytic activity of this precious metal is associated with its great hydrogen binding energy, exceptionally low overpotentials, and remarkably high exchange current density.[6,7] However, Pt cannot be mass-produced at the industrial level due to its extremely excessive scarcity and consequent costs.[8] For this reason, the use of transition metals, a class of materials much more abundant and economic, has been preferred by the industry, particularly Ni. Compared to Pt, Ni is a more affordable metal and showcases

G. G. Carvalho, M. T. Silva, M. de F. Montemor
Centro de Química Estrutural, Institute of Molecular Sciences,
Departamento de Engenharia Química
Instituto Superior Técnico, Universidade de Lisboa
Av. Rovisco Pais, 1049-001 Lisboa, Portugal
E-mail: gabriel.carvalho@tecnico.ulisboa.pt

R. E. do Nascimento
Conceção e Desenvolvimento
ISPT Industrial Services, S.A.
Av. Prof. Dr. Cavaco Silva Edifício Qualidade B2 3, 2740-120 Porto Salvo, Portugal

M. T. Silva
Unit for Innovation and Research in Engineering, ISEL
Polytechnic University of Lisbon
R. Conselheiro Emídio Navarro 1, 1959-007 Lisboa, Portugal

The ORCID identification number(s) for the author(s) of this article can be found under https://doi.org/10.1002/sstr.202400591.

DOI: 10.1002/sstr.202400591

a high performance for hydrogen evolution reactions (HER) while maintaining good stability under the cathodic regime, with the reactions nearing a heterogeneous zero-order rate which is typical of a pure catalytic behavior. Despite these advantages, the price of Ni is rising due to the high demand in the battery market.

Considering the mechanisms involved in the HER process (Volmer, Heyrovsky, Tafel steps), the cathode material deeply influences surface and/or near-surface reactions attuned to the adsorption of water molecules, formation of intermediate hydrogen ions (Volmer step), and their respective desorption with the recombination of protons into the hydrogen molecule (Heyrovsky or Tafel step).[9,10] Therefore, the binding energy of the intermediates is related to the HER performance, and Ni is a metal that remarkably stands out among the highly catalytic benchmark metals such as Pt, Pd, Au, Ir, and Ru, with a very low binding energy.[8,10–13]

Besides the reduction of costs and the optimization of the intrinsic properties of the cathode, research efforts to enhance the extrinsic properties of the electrode are also important. Conventionally, in the industrial electrolysis field, perforated metal plates have been preferred as electrodes. There are some important advantages in this 2D architecture that include good flow dynamics, tensile strength, cheap manufacturing, and high compatibility with the stack design that is widely used in industrial electrolysis.[14–16] Despite the aforementioned industrial advantages of the typical perforated electrode plates, this design is not optimal to fully harness the entirety of the deployed mass load of active material.[17] Thus, many catalytic active sites are inactive for the simple fact of being within the bulk of the electrode and consequently inaccessible by the electrolyte. This can be changed by altering the morphology and porosity of the structure of the material.

Morphologies, such as dendrites, nano and micro sheets, tubes, and foams, have been explored in the literature and proved to be capable of improving the specific surface area (SSA) of electrodes. Carbon nanostructures (e.g., graphene nanotubes, holey graphene frameworks, graphene aerogels) are commonly used as foundations for functionalization with metallic-based active materials (e.g., Ni, Mo, Fe, Ti, Mn, and respective oxides).[18,19] These nanostructured composites, which require less quantities of metal, are often synthesized by processes such as chemical vapor deposition, 3D printing, templating, or dealloying strategies that can require thermodynamically intensive steps and costly sacrificial templates.[20–22]

In contrast, a simple and low-cost synthesis technique called electrodeposition by dynamic hydrogen bubble template (DHBT) is capable of producing complex nanostructured foams, also known as nanofoams. Interestingly, this technique requires water electrolysis to produce the hydrogen necessary to form the foam and therefore the energy requirements can be also connected to a renewable source. During the foam synthesis, the electrolysis of the water molecules in the deposition electrolyte is a side reaction (Equation (1) and (2)) that competes with the electrodeposition of the metal cations (Equation (3)), forming hydrogen bubbles that serve as a self-removing template to a highly porous nanostructure, considerably optimizing the surface area:[23,24]

$$H^{+}_{(aq)} + e^{-} \rightarrow H_{(ads)} \quad (1)$$

$$2H_{(ads)} \rightarrow H_2 \quad (2)$$

$$M^{n+}_{(aq)} + ne^{-} \rightarrow M_{(s)} \quad (3)$$

DHBT electrodeposition also enables the reuse of materials recovered from urban mining, such as recycled metal salts, including Ni, chlorides, sulfates, or even hydroxides. This allows the synthesis technique to be not only integrated in a circular economy but also associated with the reuse of metal compounds that would otherwise add toxicity into battery or electronic waste and different scraps.[25–28] Using DHBT also enables the combination of different metals toward producing alloyed nanofoams (e.g., bimetallic nanofoams). The compatibility of Ni in alloying with different metals is well reported; Ni has been alloyed with other transition metals like Co, Fe, Cr, Cu, or post-transition metals such as Sn or Raney Ni.[29–33] Among these metals, Fe poses an interesting match for Ni, not only for its lower price[34] but also for its excellent electrochemical activity.[35–37] Studies show that Fe significantly lowers the charge transfer resistance in Ni-based electrodes thanks to the fast transformation of intermediate species during hydrogen evolution[33,38,39] and the acceleration of the proton discharge step, enhancing the rate-determining step toward Volmer–Heyrovsky mechanisms.[40] The presence of Fe in Ni cathodes also prevents the formation of Ni hydrides which are associated with the deactivation of the surface.[41]

It is thereby established that Fe plays a key role with Ni for improving HER due to the electrochemical synergy these two metals develop within the necessary steps of hydrogen evolution. This work focuses on the development of novel electrodes to tackle an important challenge faced by the electrolysis industry for AEL. Therefore, this work addresses the wasteful and yet unoptimized design of conventional Ni electrodes by showcasing the fabrication of Ni-based electrodes highlighting a 3D architecture with significantly higher SSA. Furthermore, these nanostructured electrodes reduce the costs of Ni utilization and the consumption of costly raw materials by replacing a significant portion of Ni with Fe, a much more abundant and eco-friendly metal, while optimizing the HER activity of the developed electrode. And finally, this work pursues the principles of the circular economy by utilizing reactants that can be obtained from urban mining (e.g., metal chlorides) obtained from the recycling of spent batteries or other devices.

2. Results and Discussion

2.1. Optimization of Fe Content in NiFe Electrodes

2.1.1. Morphology Analysis by SEM

New electrodes were synthesized aiming at an electrode material with a high surface area based on Ni due to its state-of-the-art performance for HER. Therefore, the study addresses the synthesis of Ni nanofoams by electrodeposition via DHBT, and a gradual replacement of Ni with Fe, from 100% to 40%Ni. After electrodeposition, all the produced electrodes displayed foam-like morphologies. In **Figure 1**, scanning electron

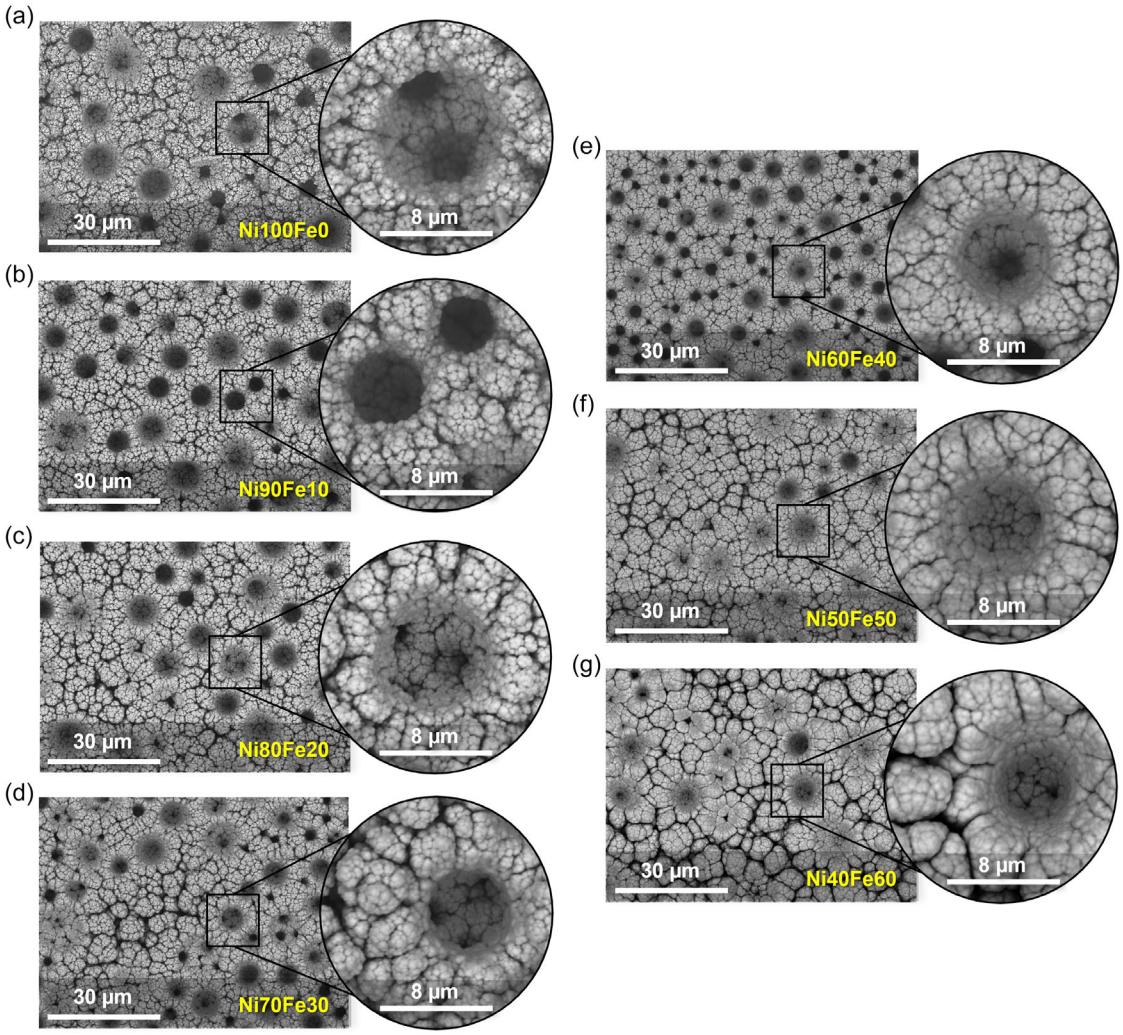

Figure 1. SEM images depicting the surface morphology of the NiFe foams synthesized with the following Ni and Fe compositions: a) $Ni_{100}Fe_0$, b) $Ni_{90}Fe_{10}$, c) $Ni_{80}Fe_{20}$, d) $Ni_{70}Fe_{30}$, e) $Ni_{60}Fe_{40}$, f) $Ni_{50}Fe_{50}$, and g) $Ni_{40}Fe_{60}$.

microscopy (SEM) images are presented (Figure 1a) for each electrodeposited NiFe nanofoam, Figure 1a–g, with Ni decreasing from 100% to 40%.

The DHBT process resulted in the formation of a porous coating, where pores of distinct size and 3D structures can be well observed. Higher Fe concentrations were not considered as these depositions resulted in very reduced porosity, loss of mechanical integrity, and consequent loss of mass upon conducting auxiliary steps such as washing, drying, and tweezers manipulation/transportation. Furthermore, a noticeable degree of surface cracking can be observed for higher concentrations of Fe as already observed in Figure 1f,g. This is well supported by a previous work where it is reported that increased Ni contents lead to foams with higher corrosion resistance and enhanced mechanical performance under tensile and bending tests.[42] The increased content of Fe in the NiFe lattice results in structural changes that facilitate and promote hydrogen diffusion and embrittlement inside the lattice, ultimately increasing cracking in the structure.[43] The single-step deposition of a bimetallic electrolyte, as is the case of NiFe, typically takes the form of an anomalous codeposition, where the less noble metal (Fe) is preferentially deposited.[44] A method that assists in exerting more control in the degree of deposition of Fe and Ni is conducting a separate deposition of Ni and Fe in different steps, or changing the electrodeposition method to a discontinued mode of operation like pulse deposition, which also averts hydrogen embrittlement by allowing hydrogen to diffuse out of the structure during the period pauses of deposition.[44,45]

2.1.2. Chemical Composition Analysis by EDS

Energy-dispersive spectroscopy (EDS) analysis of the electrodes (**Figure 2**) revealed that the resulting Ni–Fe alloys possess chemical composition similar to that of the respective deposition electrolytes, with deviations between 4 and 8% of Ni and Fe, indicating that the DHBT technique follows the target ratios between these two metals with a slight preference for Fe deposition (anomalous codeposition).[44]

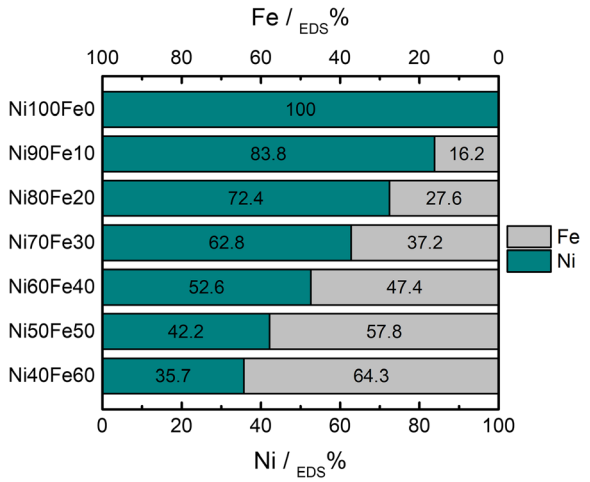

Figure 2. Chemical composition of the NiFe foams by EDS.

2.1.3. Electrochemical Behavior by LSV and Tafel Analysis

The electrochemical HER performance of each electrode was studied by linear sweep voltammetry (LSV) tests (**Figure 3**a), accompanied by their respective Tafel analysis (Figure 3b).

Noticeably in Figure 3, the results show a clear grouping of data among the NiFe foams, which suggests that Ni can be replaced by different Fe contents without compromising the electrochemical response. Despite some features that may arise when producing nanostructured Ni such as longer time required for the electrolyte to access confined pores, trapping of bubbles in the nanostructure, and compatibility of the substrate and the active material, the 3D nanostructures clearly evidence a positive effect on the electrode's electrochemical response. It is noteworthy that the activity of Ni for HER improved from the plate to the nanofoam (Ni foam) architecture. **Table 1** presents the most relevant electrochemical data ($R^2 > 0.99$) obtained from the Tafel analysis, highlighting the overpotentials measured at onset (η_{onset}) and at –10 mA cm^{-2} (η_{10}), the Tafel slopes (b), the exchange current densities (j_0), and the charge transfer coefficients (α).

The Tafel slopes of the NiFe nanofoams are within −60 to −70 mV dec^{-1} range, being less negative than the −80 mV dec^{-1} showcased by the Ni plate. This trend is in accordance with the expected range of values for ordinary industrial Ni electrodes under similar conditions, like the slope of −97 mV dec^{-1} reported by Siwek et al. for a Ni rod,[23] and the −86, −122, and −127 mV dec^{-1} reported by Zhu et al. for Ni–Sn, Raney Ni, and a Ni net, respectively.[13] These lower (absolute) values of the Tafel slopes suggest more efficient HER performance for the NiFe nanofoams. The Tafel slopes also provide information concerning the limiting steps of HER by contrasting the b values with the ranges of the known HER steps in alkaline media, presented by Equation (4)–(6):

Table 1. Kinetic parameters of electrodes of varying NiFe composition.

Electrode	η_{onset} [mV^{-1}]	η_{10} [mV^{-1}]	b [mV dec^{-1}]	$j_0 \times 10^{-7}$ A cm^{-2}	α
Ni plate	−216	−373	−80	6.38	0.74
$Ni_{100}Fe_0$	−225	−266	−61	4.39	0.94
$Ni_{90}Fe_{10}$	−188	−245	−57	6.09	1.04
$Ni_{80}Fe_{20}$	−169	−244	−60	15.4	0.99
$Ni_{70}Fe_{30}$	−161	−243	−60	18.1	0.98
$Ni_{60}Fe_{40}$	−158	−251	−60	13.9	0.99
$Ni_{50}Fe_{50}$	−155	−251	−63	18.9	0.94
$Ni_{40}Fe_{60}$	−166	−261	−68	22.9	0.87

$$H_2O + e^- + M \rightarrow MH + OH^- \quad (4)$$

$$H_2O + e^- + MH \rightarrow M + H_2 + OH^- \quad (5)$$

$$2MH \rightarrow 2M + H_2 \quad (6)$$

Each of the equations above represents a common step in the possible HER mechanisms (**Figure 4**).

Equation (4) is known as the Volmer step and defines the adsorption process of a hydrogen atom to the metallic surface at the cathode. When the process is Volmer-limited, the Tafel slope typically takes the value of ≈−120 mV dec^{-1}. After the Volmer step, two processes can occur depending on the cathode and HER conditions to which it is subject. One of such paths is the Heyrovsky step (Equation (5)) where another water molecule can react with an already adsorbed hydrogen, followed by the production of the hydrogen molecule. When HER is

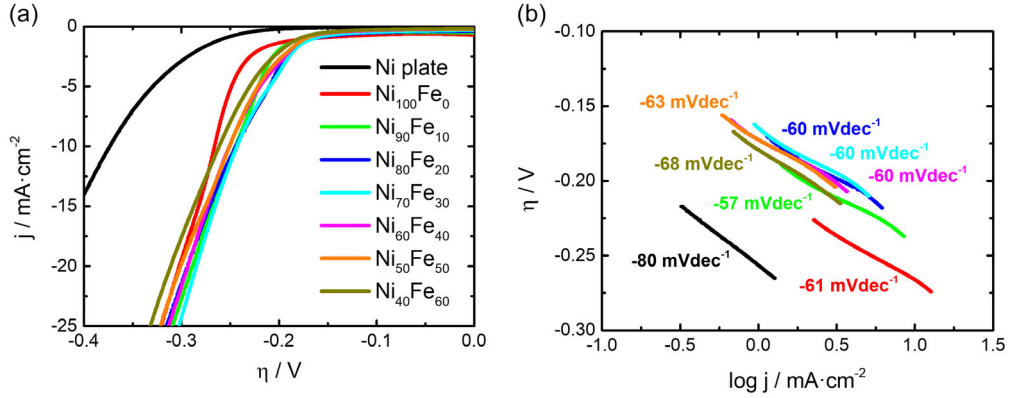

Figure 3. a) LSV curves of electrodes of varying NiFe composition and b) respective Tafel slopes.

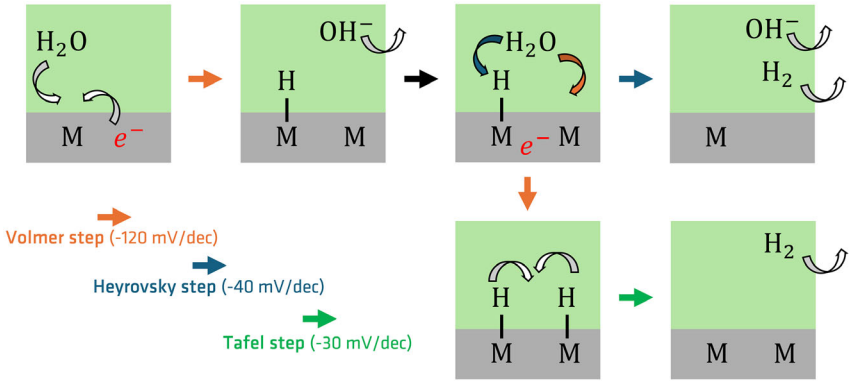

Figure 4. Visual representation of the HER mechanisms in alkaline media.

Heyrovsky-limited, the Tafel slope is ≈−40 mV dec^{-1}. The other reactional pathway is the Tafel step (Equation (6)) which produces the hydrogen molecule by combining two adsorbed hydrogen atoms. A Tafel limited process typically has a Tafel slope of ≈–30 mV dec^{-1}. It is important to note that during the HER process, all three steps occur at the cathode. What the Tafel slope analytically suggests is which one of the electrochemical steps is the limiting step of the HER process. These electrochemical fundamentals on hydrogen evolution have been intensively discussed in the literature by comprehensive reviews[46,47] and dedicated books.[48,49]

The Tafel slopes obtained in this work range from −80 to −60 mV dec^{-1}, which are within the ranges of Volmer and Heyrovsky steps, indicating that the limiting step is a combination of both steps, hence a Volmer–Heyrovsky limited HER process. These results are in accordance with the Volmer or Volmer–Heyrovsky limited HER that is often reported for transition metals, while the NiFe nanofoams showcase smaller absolute values of Tafel slopes.[50–52]

The absolute value of η_{onset} of all NiFe foams is lower than the overpotential of the Ni plate (**Figure 5**a), highlighting lower electrical demand for these cathodes when compared to the Ni plate. The Ni foam has an identical η_{onset} to the Ni plate, which is expected given that both are composed of 100%Ni. However, this similarity radically changes when comparing the overpotential measured slightly down the polarization curve (η_{10}), which is around −250 mV for all foams (Ni and NiFe alike), 100 mV better than the Ni plate (−373 mV). For this latter overpotential, the difference between the Ni foam and the Ni plate can only be explained by the extrinsic properties of each, suggesting that the 3D nanostructured morphology itself is enough to improve the overpotential of the cathode. The addition of Fe does not disturb this evolution and increases notably the current density, pointing out the benefit of Fe addition to the foams.

Figure 5b shows that the α of the NiFe foams surpassed the Ni plate and maintained high values throughout all electrodes. This is an indication that nanofoams are more electrochemically active and more sensitive to changes in overpotential. A high α value also represents the fraction of overpotential that helps lowering the free energy barrier for the reduction.[53,54]

Figure 5c represents j_0 of the foams, which increases with the Fe concentration up to the highest Fe concentration. A clear group of results can be noted with pure Ni and the lowest Fe concentration of 10%, presenting the lower values. This can be attributed to the fact that the exchange current density is an intrinsic parameter of the electrode, related solely to the composition of the active material and independent of the surface area gained from the transition from 2D to 3D morphology. Therefore, the change from a plate to a foam does not result in significant changes. The same can be stated when comparing the Ni foam with the $Ni_{90}Fe_{10}$, the lowest concentration of Fe used. The effect of Fe in this parameter is noticeable for concentrations from 20 to 40% and then increasing again for 50 and 60%.

Considering the high number of pores, good electrochemical performance, and composition of the $Ni_{60}Fe_{40}$ electrode, this specific composition was selected to undergo a durability test. Although higher Fe concentrations result in similar electrochemical performance, these samples were not considered due to the poor mechanical integrity already noticeable in the respective SEM images and previously demonstrated,[42] which most probably would limit their utilization in long-term operation.

2.1.4. Electrodes Overview and Comparison with State-of-the-Art

Having established the $Ni_{60}Fe_{40}$ electrode as the most attractive nanofoam, this electrode will hereby be referred to as the NiFe foam. **Figure 6** showcases the progression of the work, comparing the pure Ni foam with NiFe and with the industrial standard, the Ni plate.

As observed in Figure 6, two main highlights were achieved. First, the extrinsic strategy focused on developing a porous electrode with a 3D architecture produced by DHBT using the same material used as the industrial standard, Ni. This approach led to a significant improvement of the electrochemical performance, as the absolute values of the η_{10} and Tafel slopes were reduced from −373 to −266 mV and −80 to −61 mV dec^{-1}, respectively. Second, the NiFe nanofoam, in which 40% of Ni was replaced by Fe, resulted in slightly improved activity for hydrogen evolution. This is evidenced by an absolute drop of the η_{10} from −266 to −251 mV and unaltered the Tafel slopes, suggesting no changes in the hydrogen evolution mechanisms. The electrochemical data (overpotential at −10 mA cm^{-2} and Tafel slopes) related to these electrodes are compared to the state-of-the-art on Ni-based electrodes for AEL in **Table 2**.

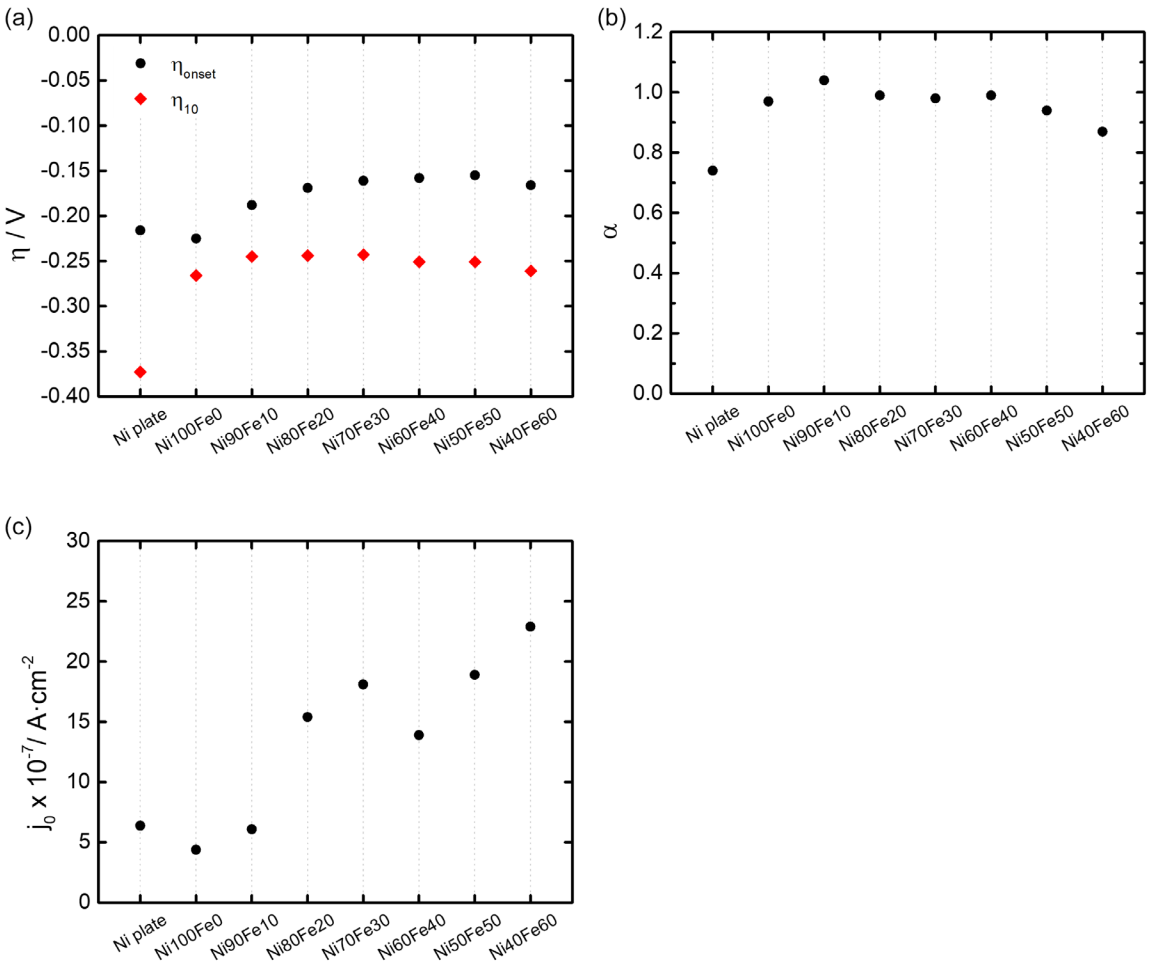

Figure 5. a) Overpotential at onset and $-10\,\mathrm{mAcm^{-2}}$; b) charge transfer coefficient; and c) exchange current density.

A comparison to recent literature on Ni-based electrodes (Table 2) suggests a very promising placement of the developed NiFe electrode, showcasing overpotentials within the expected range (≈ -200 mV) while significantly improving the Tafel slopes, holding a value of $-60\,\mathrm{mV\,dec^{-1}}$ which is practically half the average slope of the referenced literature ($\approx -126\,\mathrm{mV\,dec^{-1}}$). The good electrochemical performance of the NiFe electrode can be attributed to some synergies created between Ni and Fe. As previously mentioned, some electrochemical advantages can be attributed to the role of Fe in HER mechanisms. Proton discharge (Tafel step) is preferential in the active Fe atoms, and therefore their presence in Ni foam significantly accelerates the charge transfer from Ni to Fe.[40] Demnitz et al. also showed that Fe is associated with the formation of dendrite layers detected in Ni lattices, increasing the surface area and effectively preventing the formation of Ni hydrides (NiH_x) which deactivate the surface.[41] NiFe alloys are reported to exhibit higher electric conductivity than pure Ni or Fe.[40,55,56] Such is the case of permalloys (bimetallic alloys of 80% Ni and 20% Fe) widely used for thermal, magnetic, and electronic applications.[57,58] In their work, Avery et al. provided a detailed and precise estimation of the thermal conductivity with measured electrical conductivity and highlighted the resilience of NiFe across the studied temperature range, while other metals (i.e., Al, Cu, Co) revealed shorter ranges of operation.[57] Zhang et al. presented a comprehensive characterization study of the magnetic, optical, and electrical properties of NiFe, demonstrating the connection between this properties and the

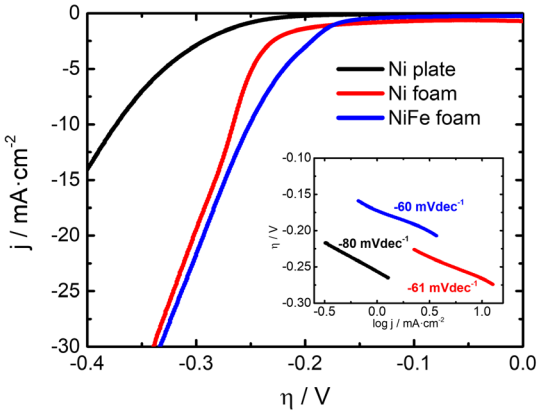

Figure 6. LSVs and Tafel slopes (inset) of the Ni plate, Ni foam, and $Ni_{60}Fe_{40}$ foam.

Table 2. Comparison of HER electrodes reported by literature with electrodes developed by this work.

Electrode	Synth. method	Electrolyte	η_{10}[a)] [mV^{-1}]	b [mV dec^{-1}]	References
Ni plate	–	30 wt% KOH	−373	−80	This work
Ni foam	DHBT	30 wt% KOH	−266	−62	This work
NiFe foam	DHBT	30 wt% KOH	−251	−60	This work
Ni foam	DHBT	8.0 M KOH	−188	−160	[23]
Ni–Co@Ni mesh	Electroless-plating	30 wt% KOH	−225	99	[29]
Ni–Cu@Ni foam	Electrodeposition	1.0 M KOH	−202	−82	[31]
Ni–Cr–Fe	Sintering	6.0 M KOH	−261	−202	[33]
NiO NS[b)]	CBD[c)]	1.0 M KOH	−214	−105	[38]
Fe-doped NiO NS	CBD	1.0 M KOH	−177	−108	[38]

[a)]Some overpotentials were estimated from LSV to maintain the reference at −10 mA cm^{-2}. [b)]Nanosheets. [c)]Chemical bath deposition.

crystalline structure of the NiFe.[58] There is a higher density of active sites when Fe is present in the Ni lattice, enhancing the adsorption and reduction steps of HER.[59] Fe can provoke a redistribution of the charge density in an NiFe alloy, optimizing the electronic structure across the electrode surface, enabling stronger interactions for hydrogen evolution.[60,61] Another attribute of NiFe alloys is the ability to form mixed oxides and hydroxides, such as layered double hydroxides, which increase the catalytic activity while retaining good chemical stability even under the cathodic regime of hydrogen evolution.[62,63] The formation of oxides and hydroxides is a typical phenomenon commonly present in AEL; however, for the case of the presented electrodes, any formation of MOHs that might have occurred was not detected probably due to their reduction under the cathodic regime.

Many of these synergies can be attributed to the similarity of the chemical and physical properties of Ni and Fe, such as atomic mass, electronic configuration, ionization energy, oxidation states, and others, which can be extensively explored in handbooks like Davis et al.[64] These observations clearly evidence the positive role of Fe that is further demonstrated in this work when used to replace Ni in a 3D foam architecture.

2.1.5. Durability Assessment

The durability test is shown in **Figure 7**a, performed by chronopotentiometry (CP) for 60 h at a constant current density of −10 mA cm^{-2} which was selected for comparative purposes between the measured potentials during the CP and the η_{10} measured in the LSV conducted before and after durability test. Figure 7b highlights the LSV of the electrode before and after the CP, accompanied by the respective Tafel slopes as figure inset. **Table 3** presents the electrochemical data obtained from LSV and Tafel analysis

The CP (Figure 7a) shows a stable plateau throughout the 60 h of testing, with a final potential retention of 93,4%. As the inset of Figure 7a highlights, after an initial decay of 2 h, the overpotential stabilizes. This indicates that the NiFe electrodes can sustain their performance effectively, retaining most of its initial characteristics throughout the testing period. Table 3 presents the electrochemical data before and after the CP via LSV, and, considering the absolute value of the overpotentials and Tafel slopes, the analysis of the LSV curves (Figure 7b) reveals increased overpotentials and Tafel slopes and practically unchanged α and j_0.

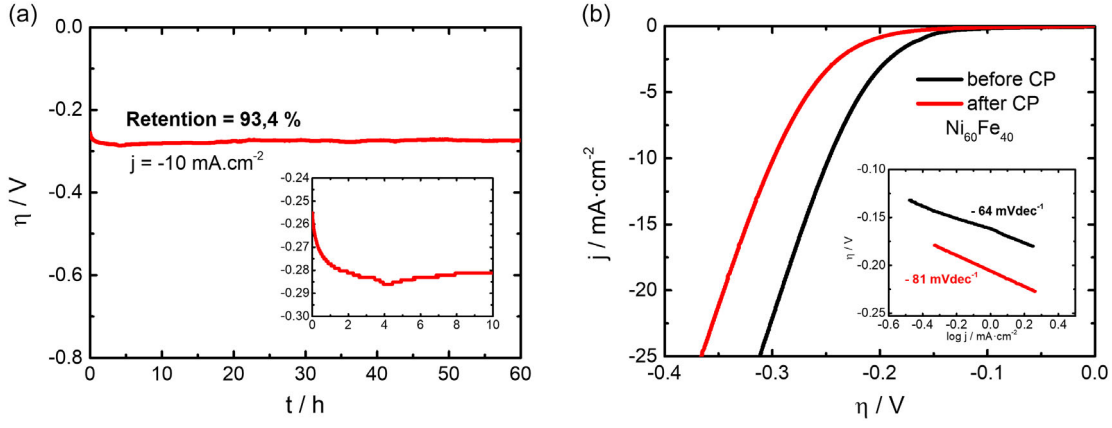

Figure 7. Durability test on the $Ni_{60}Fe_{40}$ electrode: a) CP of 60 h with the first 10 h as inset and b) LSV and Tafel slopes (inset) for before and after the CP.

Table 3. Electrochemical data of the $Ni_{60}Fe_{40}$ electrode before and after CP.

NiFe[a)]	η_{onset} [mV^{-1}]	η_{10} [mV^{-1}]	b [$mV\,dec^{-1}$]	$j_0 \times 10^{-7}$ $A\,cm^{-2}$	α
Before CP	−131	−247	−64	26.9	0.99
After CP	−178	−299	−81	29.5	0.99

[a)]Synthesized under the same conditions of the previously studied $Ni_{60}Fe_{40}$ nanofoam.

The initial η_{10} of −247 mV increased to −299 mV. This suggests that the electrode suffered a performance degradation and now requires more energy to produce the same amount of H_2 (i.e., the same current density). Ideally, these values should be identical to the first and last overpotentials measured during the CP: −255 and −273 mV, respectively. The difference between the values recorded in the CP and LSVs is most likely associated with the operating conditions of the applied techniques, namely, the fact that the CP maintains a constant current density of $-10\,mA\,cm^{-2}$ throughout the test while during a LSV the current density varies across the programmed potential sweep. Nevertheless, considering the proximity of the values and the context of the durability analysis, these differences were deemed negligible and primarily attributed to the operating conditions of the conducted tests, and only the values before and after the durability test were considered for further comparison. The increased Tafel slopes also indicate a slightly decreased efficiency for HER after the CP. The evolution from −64 to $-82\,mV\,dec^{-1}$ suggests that despite the HER mechanisms suffering a decay $18\,mV\,dec^{-1}$ the electrode was able to maintain its Heyrovsky–Volmer limited reaction. On the other hand, the α value before and after the durability test remained very high (0.99) when compared to the value of 0.5 which is generally considered by the literature as representative of a typical balanced contribution of applied overpotential in electrodes and is often the value assumed a priori for other methods of electrochemical analysis.[53,54] Moreover, considering that there are no significant changes in j_0, the values of these two key parameters evidence that the electrode maintained good electrochemical response at its equilibrium state: continuing to be highly sensitive to the reactants (α) and maintaining its tendency for redox reactions (j_0).

In summary, the electrochemical results primarily suggest that after the CP the electrode requires more energy to enable HER (more negative overpotentials) while simultaneously evolving toward less efficient HER mechanisms (more negative Tafel slopes). This might be associated with the formation of transition metal oxides and hydroxides that are known to lower the conductivity and activity of the material.[34,36,62,65,66] Additionally, SEM and EDS analysis also evidenced that the electrode surface remained unchanged after the CP, suggesting that the slight decay might be associated with other factors, such as minor surface passivation and subtle surface changes at the atomic scale.

3. Conclusions

Different compositions of Ni and Fe were studied for the synthesis of porous NiFe electrodes by DHBT electrodeposition onto stainless-steel substrates. The synthesis process yields materials with compositions that were in good agreement with the compositions of the deposition electrolytes. A notable distribution of pores was observed for all nanofoams, with the higher number of pores obtained for the $Ni_{60}Fe_{40}$ electrode. The NiFe nanofoams showcased better electrochemical performance for HER compared to pure Ni plates and foams and in general follow Volmer–Heyrovsky limited mechanisms. High charge transfer coefficients were determined for all electrodes, evidencing the irreversibility of the electrodes toward the reduction reaction, while the highest obtained exchange currents occur for electrodes with higher Fe concentration. These results demonstrate that $Ni_{60}Fe_{40}$ nanofoams which present a very porous architecture, good electrochemical performance, including after the ageing tests, and potentially good mechanical stability can replace pure Ni plates by improving the HER activity and reducing material costs with the use of cheaper substrates and more affordable metals in the synthesis of metallic foams. These improvements are associated with both extrinsic and intrinsic properties of the NiFe nanofoams, like the 3D architecture and the synergy between Ni and Fe toward HER when combined in the bimetallic nanofoam.

4. Experimental Section

Electrodeposition by DHBT: NiFe nanofoams were electrodeposited under the DHBT cathodic regime from electrolytes with different concentrations of Ni and Fe precursors. All electrolytes were prepared from a base of ammonia chloride (NH_4Cl, Sigma–Aldrich, ≥99.5 wt%) and citric acid ($C_6H_8O_7$, Carl Roth, ≥99.0 wt%) with varying compositions of nickel chloride ($NiCl_2.6H_2O$, Carl Roth, ≥98.0 wt%) and iron chloride ($FeCl_3.6H_2O$, Carl Roth, ≥99.0 wt%), maintaining a total concentration of metals of 0.1 M. Electrodes with different compositions of NiFe were prepared and labeled as $Ni_{\%Ni}Fe_{\%Fe}$ for their respective electrolyte composition, and were the following: $Ni_{100}Fe_0$, $Ni_{90}Fe_{10}$, $Ni_{80}Fe_{20}$, $Ni_{70}Fe_{30}$, $Ni_{60}Fe_{40}$, $Ni_{50}Fe_{50}$, and $Ni_{40}Fe_{60}$.

For the electrodeposition, a stainless-steel substrate (plate and grid design) was used as the working electrode and a graphite plate as the counter-electrode, connected to an energy source (BX PRECISION model 1688B) which maintained a current density of $-1\,A\,cm^{-2}$ for a geometric area of deposition of $1.54\,cm^2$ during 150 s. The morphology of all the prepared electrodes was characterized by optical microscopy (Leica DM 2700 M of Leica Microsystems), SEM, and the respective composition by EDS mode coupled in the same device (Phenom Desktop SEM of Thermo Fisher Scientific).

Electrochemical Tests: LSV and CP were conducted at room temperature and pressure in an alkaline media of potassium hydroxide (KOH, Carl Roth, ≥85.0 wt%) at the concentration of 30 wt%, as it is commonly used in the industrial setting. A three electrodes' electrochemical cell was used with a graphite plate serving as a counter electrode and the Hg/HgO electrode as reference. LSV was conducted at a scan rate of $1\,mV\,s^{-1}$ within a potential window from OCP to −1.4 V versus Hg/HgO. All potentials were converted from the experimental reference of Hg/HgO to the reversible hydrogen electrode (RHE) potential by applying Equation (7):

$$E_{RHE} = E_{Hg/HgO} + E_{0,\,Hg/HgO} + \frac{In\,(10)\,RT}{F}pH \tag{7}$$

where E_{RHE} is the potential converted to RHE, $E_{Hg/HgO}$ is the potential versus Hg/HgO, $E_{0,\,Hg/HgO}$ is the standard potential for Hg/HgO, R is the perfect gas constant, T is the temperature, and F is the Faraday's constant.

Acknowledgements

The authors acknowledge the support of ISPT—Industrial Services, S.A. as nonacademic host institution and the funding from Fundação para a Ciência e a Tecnologia (FCT) through the grant reference 2022.13366.BDANA. Centro de Química Estrutural is a research unit funded by Fundação para a Ciência e a Tecnologia through projects UIDB/00100/2020 and UIDP/00100/2020, DOI 10.54499/UIDP/00100/2020 and DOI 10.54499/UIDP/00100/2020. Institute of Molecular Sciences is an associate laboratory funded by FCT through project LA/P/0056/2020, DOI 10.54499/PTDC/QUI-ELT/2075/2020.

Conflict of Interest

The authors declare no conflict of interest.

Author Contributions

Gabriel Garcia Carvalho: conceptualization: (lead); investigation: (lead); methodology: (lead); writing—original draft: (lead); writing—review and editing: (equal). **Ricardo Espingardas do Nascimento**: investigation: (supporting); resources: (supporting); supervision: (equal); validation: (supporting); writing—original draft: (supporting); writing—review and editing: (equal). **Maria Teresa Silva**: conceptualization: (supporting); investigation: (supporting); supervision: (equal); writing—original draft: (supporting); writing—review and editing: (equal). **Maria de Fátima Montemor**: conceptualization: (supporting); funding acquisition: (lead); investigation: (supporting); resources: (lead); supervision: (lead); validation: (lead); writing—original draft: (supporting); writing—review and editing: (equal).

Data Availability Statement

The data that support the findings of this study are available from the corresponding author upon reasonable request.

Keywords

alkaline electrolysis, dynamic hydrogen bubble template electrodeposition, hydrogen evolution, nanofoams, nickel–iron

Received: November 7, 2024
Revised: January 15, 2025
Published online:

[1] M. I. Khzouz, E. Gkanas, in *Renewable Energy - Resources, Challenges and Applications* (Eds: M. Al Qubeissi, A. El-kharouf, H. Serhad Soyhan), IntechOpen, London **2020**.
[2] E. B. Agyekum, C. Nutakor, A. M. Agwa, S. A. Kamel, *Membranes* **2022**, *12*, 173.
[3] IEA, *Global Hydrogen Review 2023*, IEA, Paris **2023**, https://www.iea.org/reports/global-hydrogen-review-2023
[4] A. Sh. Aliyev, R. G. Guseynova, U. M. Gurbanova, D. M. Babanly, V. N. Fateev, I. V. Pushkareva, D. B. Tagiyev, *Chem. Probl.* **2018**, *16*, 283.
[5] A. Hodges, A. L. Hoang, G. Tsekouras, K. Wagner, C. Y. Lee, G. F. Swiegers, G. G. Wallace, *Nat. Commun.* **2022**, *13*, 1304.
[6] Q. Yu, Z. Zhang, H. Liu, X. kang, S. Ge, S. Li, L. Gan, B. Liu, *Fundam. Res.* **2023**, *3*, 804.
[7] F. Guo, T. J. Macdonald, A. J. Sobrido, L. Liu, J. Feng, G. He, *Adv. Sci.* **2023**, *10*, 2301098.
[8] B. He, Y. Kuang, Z. Hou, M. Zhou, X. Chen, *J. Mater. Res.* **2018**, *33*, 213.
[9] G. G. Carvalho, S. Eugénio, M. T. Silva, M. F. Montemor, *Batteries* **2022**, *8*, 37.
[10] L. Huo, C. Jin, K. Jiang, Q. Bao, Z. Hu, J. Chu, *Adv. Energy Sustain. Res.* **2022**, *3*, 2100189.
[11] L. Dheer, S. Bhattacharjee, S. C. Lee, U. V. Waghmare, *Mater. Res. Express* **2019**, *6*, 124006.
[12] A. Raveendran, M. Chandran, R. Dhanusuraman, *RSC Adv.* **2023**, *13*, 3843.
[13] Y. Zhu, T. Liu, L. Li, S. Song, R. Ding, *Ionics* **2018**, *24*, 1121.
[14] M. Selt, B. Gleede, R. Franke, A. Stenglein, S. R. Waldvogel, *J. Flow Chem.* **2021**, *11*, 143.
[15] A. Rearden, S. Mandale, K. Glover, R. Phillips, C. W. Dunnill, *Arch. Chem. Chem. Eng.* **2020**, *2*, 1.
[16] D. M. F. Santos, C. A. C. Sequeira, D. Macciò, A. Saccone, J. L. Figueiredo, *Int. J. Hydrogen Energy* **2013**, *38*, 3137.
[17] J. Koj, C. Wulf, A. Schreiber, P. Zapp, *Energies* **2017**, *10*, 860.
[18] H. Sun, J. Zhu, D. Baumann, L. Peng, Y. Xu, I. Shakir, Y. huang, X. Duan, *Nat. Rev. Mater.* **2018**, *4*, 45.
[19] Z. Yu, L. Tetard, L. Zhai, J. Thomas, *Energy Environ. Sci.* **2015**, *8*, 702.
[20] B. Jiang, C. He, N. Zhao, P. Nssh, C. Shi, Z. Wang, *Sci. Rep.* **2015**, *5*, 13825.
[21] P. Kubelka, F. Körte, J. Heimann, X. Xiong, N. Jost, *Adv. Eng. Mater.* **2022**, *24*, 2100608.
[22] A. Zahoor, A.-H. I. Mourad, S. Husain Khan, in *Advances in Science and Engineering Technology Inter. Conf. (ASET)*, IEEE, Dubai, United Arab Emirates **2022**, pp. 1–6.
[23] K. I. Siwek, S. Eugénio, D. M. F. Santos, M. T. Silva, M. F. Montemor, *Int. J. Hydrogen Energy* **2019**, *44*, 1701.
[24] P. Arévalo-Cid, A. Adán-Más, T. M. Silva, J. A. Rodrigues, E. Maçôas, M. F. Vaz, M. F. Montemor, *Mater. Charact.* **2020**, *169*, 110598.
[25] C. Tunsu, M. Petranikova, M. Gergorić, C. Ekberg, T. Retegan, *Hydrometallurgy* **2015**, *156*, 239.
[26] M. Wang, Q. Tan, J. F. Chiang, J. Li, *Front. Environ. Sci. Eng.* **2017**, *11*, 1.
[27] D. Prodius, K. Gandha, A.-V. Mudring, I. C. Nlebedim, *ACS Sustain. Chem. Eng.* **2020**, *8*, 1455.
[28] W. Begum, S. Rai, S. Banerjee, S. Bhattacharjee, M. H. Mondal, A. Bhattarai, B. Saha, *RSC Adv.* **2022**, *12*, 9139.
[29] F. J. Pérez-Alonso, C. Adán, S. Rojas, M. A. Peña, J. L. G. Fierro, *Int. J. Hydrogen Energy* **2015**, *40*, 51.
[30] H. H. Shaarawy, H. S. Hussein, A. Attia, S. I. Hawash, *Environ. Sci. Pollut. Res.* **2024**, *31*, 28719.
[31] N. Lotfi, T. Shahrabi, Y. Yaghoubinezhad, G. B. Darband, *J. Electroanal. Chem.* **2019**, *848*, 113350.
[32] K. Ngamlerdpokin, N. Tantavichet, *Int. J. Hydrogen Energy* **2014**, *39*, 2505.
[33] L. Wu, G. Yang, Z. Li, Y. Xiao, J. Qian, Q. Zhang, J. Huang, *RSC Adv.* **2020**, *10*, 44933.
[34] H. Sun, W. Jung, *J. Mater. Chem. A* **2021**, *9*, 15506.
[35] X. Cao, T. Wang, L. Jiao, *Adv. Fiber Mater.* **2021**, *3*, 210.
[36] B. W. Xue, C. H. Zhang, Y. Z. Wang, W. W. Xie, N. W. Li, L. Yu, *Nanoscale Adv.* **2020**, *2*, 5555.
[37] Y. Messaoudi, H. Belhadj, M. R. Khelladi, A. Azizi, *RSC Adv.* **2022**, *12*, 29143.
[38] Z. Qiu, Y. Ma, G. A. Niklasson, T. Edvinsson, *Physchem* **2021**, *1*, 69.
[39] Z. Chen, Q. Li, H. Xiang, Y. Wang, P. Yang, C. Dai, H. Zhang, W. Xiao, Z. Wu, L. Wang, *Inorg. Chem. Front.* **2023**, *10*, 1234.
[40] S. Meguro, T. Sasaki, H. Katagiri, H. Habazaki, A. Kawashim, T. Sakaki, K. Asami, K. Hashimoto, *J. Electrochem. Soc.* **2000**, *147*, 3003.
[41] M. Demnitz, Y. M. Lamas, R. L. G. Barros, A. D. Den Bouter, J. van der Schaaf, M. T. De Groot, *IScience* **2024**, *27*, 108695.

[42] P. Arévalo-Cid, M. F. Vaz, M. F. Montemor, *Mater. Charact.* **2022**, *193*, 112311.
[43] D. Sobola, R. Dallaev, *Energies* **2024**, *17*, 2972.
[44] Y. Wang, N. Williamson, R. Dawson, N. Bimbo, *J. Appl. Electrochem.* **2023**, *53*, 877.
[45] V. Meinhold, D. Höhlich, T. Mehner, T. Lampke, *Coatings* **2022**, *12*, 56.
[46] C. A. Campos-Roldán, N. Alonso-Vante, *Electrochem. Energy Rev.* **2019**, *2*, 312.
[47] M. Ďurovič, J. Hnát, K. Bouzek, *J. Power Sources* **2021**, *493*, 229708.
[48] A. Lasia, *Handb. Fuel Cells* **2010**, *2*, 416.
[49] P. K. Dutta, S. A. Akbar, in *Encyclopedia of Applied Electrochemistry* (Eds: G. Kreysa, K. Ota, R. F. Savinell), Springer New York, New York, NY **2014**, pp. 973–981.
[50] N. A. Kamaruzaman, W. M. K. Wan Mohamed Zin, K. H. Kamarudin, N. M. Saleh, F. Yusoff, *Int. J. Electrochem. Sci.* **2023**, *18*, 100187.
[51] M. N. Lakhan, A. Hanan, A. H. Shar, I. Ali, Y. Wang, M. Ahmed, U. Aftab, H. Sun, H. Arandiyan, *Chem. Commun.* **2024**, *60*, 5104.
[52] J. Li, Z. Jing, H. Bai, Z. Chen, A. I. Osman, M. Farghali, D. W. Rooney, P. S. Yap, *Environ. Chem. Lett.* **2023**, *21*, 2583.
[53] R. Guidelli, R. G. Compton, J. M. Feliu, E. Gileadi, J. Lipkowski, W. Schmickler, S. Trasatti, *Pure Appl. Chem.* **2014**, *86*, 245.
[54] R. Maurya, R. Das, A. K. Tripathi, M. Neergat, *Phys. Chem. Chem. Phys.* **2023**, *25*, 700.
[55] N. Mahmood, Y. Yao, J. W. Zhang, L. Pan, X. Zhang, J. J. Zou, *Adv. Sci.* **2018**, *5*, 1700464.
[56] G. Shi, C. Arata, D. A. Tryk, T. Tano, M. Yamaguchi, A. Liyama, M. Uchida, K. Lida, S. Watanabe, K. Kakinuma, *ACS Omega* **2023**, *8*, 13068.
[57] A. D. Avery, S. J. Mason, D. Bassett, D. Wesenberg, B. L. Zink, *Phys. Rev. B* **2015**, *92*, 214410.
[58] M. Zhang, C. Deng, *J. Mater. Sci. Mater. Electron.* **2021**, *32*, 494.
[59] M. Drosou, F. Kamatsos, C. A. Mitsopoulou, *Inorg. Chem. Front.* **2020**, *7*, 37.
[60] N. K. Oh, J. Seo, S. Lee, H. J. Kim, U. Kim, J. Lee, Y. K. Han, H. Park, *Nat. Commun.* **2021**, *12*, 4606.
[61] Q. Kang, D. Lai, W. Tang, Q. Lu, F. Gao, *Chem. Sci.* **2021**, *12*, 3818.
[62] M. S. S. Danish, *RSC Sustain.* **2023**, *1*, 2180.
[63] T. Li, W. Liu, H. Xin, Q. Sha, H. Xu, Y. Kuang, X. Sun, *Catalysts* **2024**, *14*, 296.
[64] J. R. Davis, *ASM Specialty Handbook Nickel, Cobalt, and Their Alloys*, ASM International, Materials Park, OH **2000**.
[65] J.-D. He, H.-D. Wang, X.-M. Zang, L. Huang, Y. Li, L. Xia, C.-R. Pi, J.-P. Li, Y. Zheng, B. Gao, K.-F. Huo, *Rare Met.* **2024**.
[66] M. Luo, J. Yang, X. Li, M. Eguchi, Y. Yamauchi, Z. L. Wang, *Chem. Sci.* **2023**, *14*, 3400.